Progress in Solid State Chemistry 76 (2024) 100494

Contents lists available at ScienceDirect

Progress in Solid State Chemistry

journal homepage: www.elsevier.com/locate/pssc

New solid solutions with the *R*-type hexaferrite structure, $BaFe_{4-x}M_xM'_2O_{11}$ (M = In, Sc; M' = Ti, Sn)

Yu-An Huang [a], Jun Li [a], Arthur P. Ramirez [b], M.A. Subramanian [a,*]

[a] Department of Chemistry, Oregon State University, Corvallis, OR, 97331, USA
[b] Department of Physics, University of California, Santa Cruz, CA, 95064, USA

ARTICLE INFO

Keywords:
Hexaferrites
R-type ferrite
Reflectivity
Soft magnetic material
Heat-reflective material

ABSTRACT

Hexaferrites are a family of complex iron oxides with hexagonal structures. Novel compositions with the *R*-type hexaferrite structure, $BaFe_{4-x}M_xM'_2O_{11}$ (M = In, Sc; M' = Ti, Sn; x = 0.0–1.8), are synthesized and characterized. Structural analyses using powder neutron diffraction reveal that trivalent iron cations are distributed among all the available M sites (octahedral and trigonal bipyramidal sites), with site preference varying with the composition. Ferrimagnetic behavior is observed for all the compounds, and the observed magnetic hysteresis loop indicates that the compounds are soft magnets. The color of the new solid solution can be tuned from dark reddish brown to reddish-orange and yellowish-orange as In or Sc substitutions increase. The origin of colors in these ferrite-based solid solutions results from the combination of ligand-to-metal charge transfer and electron-pair transitions across the face-shared octahedra, as seen in the hematite (Fe_2O_3). Reducing Fe content in the parent compound improves the diffuse reflectance in the near-infrared range, suggesting potential applications as cool pigments.

1. Introduction

The hexaferrite family consists of ferrites with hexagonal structures and crystallizes in the $P6_3/mmc$ space group. Common hexaferrite types include M-type ($AM_{12}O_{19}$), Z-type ($A_3M'_2M_{24}O_{41}$), Y-type ($A_2M'_2M_{12}O_{22}$), W-type ($AM'_2M_{16}O_{27}$), X-type ($A_2M'_2M_{28}O_{46}$), and U-type ($A_4M'_2M_{36}O_{60}$). These different structure types can be described by the individual basic formulas and the different stacking orders of S-block (spinel block), R-block, and T-block [1,2]. The most well-studied hexaferrite is the M-type barium hexaferrite ($BaFe_{12}O_{19}$), which is a strong room-temperature ferrimagnetic material where iron occupies octahedral, tetrahedral, and trigonal bipyramidal (TBP) sites [1,3]. Furthermore, the hexaferrite family of compounds is found widely useful in many areas, such as magnetic recording, data storage, magnetic separators, electrical devices, magnetoelectric materials, and microwave-absorbing applications [2,4,5]. However, the optical properties of the hexaferrite series are rarely explored [6].

In addition to the commonly known hexaferrite types, a distinct *R*-type ferrite system exists. The structure of *R*-type hexaferrite has the basic formula of $AM^{3+}{}_4M'^{4+}_2O_{11}$, where A site is occupied by a divalent cation, M site is occupied by a trivalent cation, and M' site is occupied by a tetravalent cation. The M and M' cations are located at the octahedral and TBP sites. The major difference between the *R*-type hexaferrite ($AM_4M'_2O_{11}$) and the normal M-type hexaferrite ($AM_{12}O_{19}$) is the stacking sequence of M cation sites and the absence of tetrahedral coordination in the *R*-type structure. In the *R*-type structure, there are RR*RR* stackings, while in the normal hexaferrite structure, the sequence is SRS*R* with S-block and R-block stacking alternatively along the *c*-axis (Fig. 1). One particular *R*-type compound of interest is $BaFe_4Ti_2O_{11}$, which has been shown to exhibit ferrimagnetic behavior, likely due to site mixing between Fe^{3+} and Ti^{4+} [7–9]. The *R*-type hexaferrite structure holds considerable interest in investigating the relationship between the structure and properties.

Inorganic pigments that can exhibit high reflectivity in the near-IR region have gained increased importance in light of climate change-related concerns, particularly with regard to global warming. High heat-reflecting surfaces can be attained using heat-reflective coatings that incorporate inorganic color pigments with high reflectivity in near-IR regions. Increasing the solar reflectance of building roofs, walls, and surroundings (e.g., pavements) reduces power demand during peak hours by decreasing the need for air conditioning in hot weather. Based on the refined crystal structures of hexagonal ferrite-related compounds

* Corresponding author.
E-mail address: Mas.Subramanian@oregonstate.edu (M.A. Subramanian).

https://doi.org/10.1016/j.progsolidstchem.2024.100494
Received 23 October 2024; Received in revised form 4 November 2024; Accepted 6 November 2024
Available online 8 November 2024

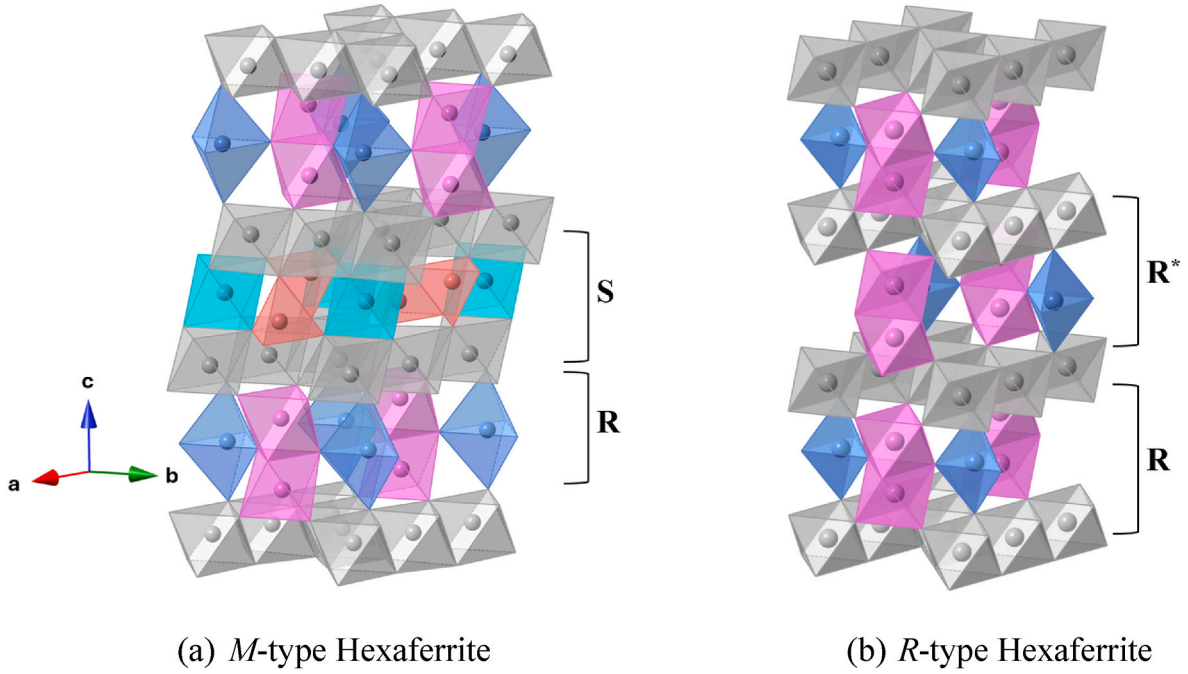

Fig. 1. The normal *M*-type and the *R*-type hexaferrite structures are shown using compounds (a) $BaFe_{12}O_{19}$ and (b) $BaFe_4Ti_2O_{11}$, respectively. Symmetrically distinct *M*/*M*′ sites are shown in different colors: (a) *M*-type: turquoise (*2a*) and grey (*12k*): edge-shared octahedral; pink (*4f*): face-shared octahedral; brick red (*4f*): tetrahedral; blue (*2b*): TBP. (b) *R*-type: grey (*6g*): edge-shared octahedral; pink (*4e*): face-shared octahedral; blue (*2d*): TBP.

such as hibonites ($CaAl_{12}O_{19}$), the transition metal chromophores are distributed mainly in tetrahedral and trigonal bipyramidal (TBP) sites [10–12]. According to the Laporte selection rules, materials with TBP and tetrahedral sites with no inversion center are ideal candidates for observing intense colors [13]. The YInMn blue (hexagonal $YIn_{1-x}Mn_xO_3$ solid solutions) and cobalt blue (spinel $CoAl_2O_4$) give excellent examples of how TBP and tetrahedral coordinations can significantly impact the color of the samples [14–16].

In this paper, we report on the synthesis and characterization of $BaFe_{4-x}M_xM'_2O_{11}$ (*M* = In, Sc; *M*′ = Ti, Sn) with an *R*-type hexaferrite structure and show how cation distributions impact the magnetic and color properties.

2. Experimental procedure

2.1. Synthesis

Samples of indium-substituted *R*-type hexaferrite with the general formula $BaFe_{4-x}M_xM'_2O_{11}$ (*M* = In, Sc; *M*′ = Ti, Sn; $0 \leq x \leq 1.8$) were prepared by standard solid-state reactions. A stoichiometric mixture of $BaCO_3$ (Alfa Aesar, 99.997 %), Fe_2O_3 (Alfa Aesar, 99.945 %), In_2O_3 (Indium Corp. of America, 99.99 %), Sc_2O_3 (Sigma-Aldrich, 99.9 %) and TiO_2 (Aldrich, 99.9 %) or SnO_2 (Sigma-Aldrich, 99.9 %) was ground in an agate mortar with a pestle. The $BaCO_3$ powder was dried overnight under 120 °C before being weighed. The precursor powder was then pressed into pellets with an applied pressure of 1 psi. The pellets were then put in alumina crucibles and heated at 1100 °C for 24–30 h in the air with intermediate grindings until the single phase was obtained.

2.2. Characterization

Phase identification was performed using a Rigaku Miniflex II desktop diffractometer to identify the purity of the samples with Cu Kα radiation and a graphite monochromator on the diffracted beam. The X-ray diffraction data were collected over 2θ within a range of 10–70° at room temperature. The unit cell parameters were refined using GSAS/EXPGUI software package [17]. For additional structural analysis, the

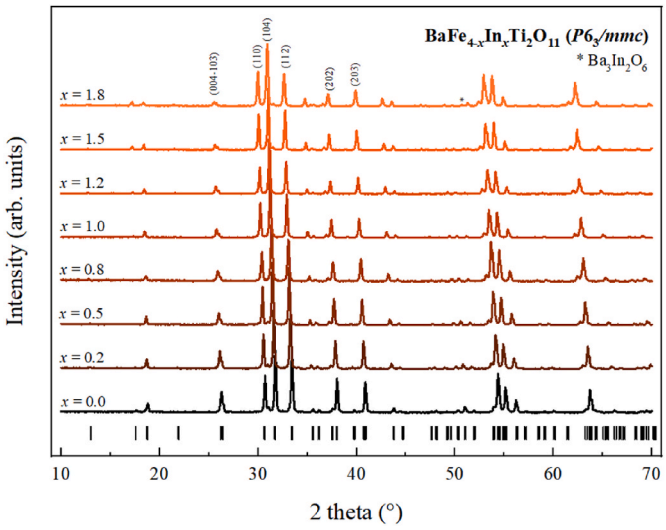

Fig. 2. Powder X-ray diffraction patterns of $BaFe_{4-x}In_xTi_2O_{11}$ ($x = 0.0 - 1.8$) samples. The impurity can be observed above $x = 1.5$.

neutron diffraction data for $BaFe_3InTi_2O_{11}$ and $BaFe_3InSn_2O_{11}$ samples were collected from the Spallation Neutron Source (SNS) BL-11A POWGEN beamline at Oak Ridge National Laboratory (ORNL). The samples were packed in an 8 mm width vanadium container with 70 mm height. Time of flight (TOF) neutron data were obtained at room temperature over 11–200° range of 2θ. Rietveld refinements of the crystal structures were performed using the GSAS software with the EXPGUI interface [17,18].

Magnetization data were measured using Quantum Design MPMS3 from 5 to 300 K. Magnetization hysteresis data were obtained between −2 T and 2 T Oe magnetic field.

The diffuse reflectance data of powder samples were collected with the Jasco V-670/V-770 UV–vis Near IR spectrophotometer. The data

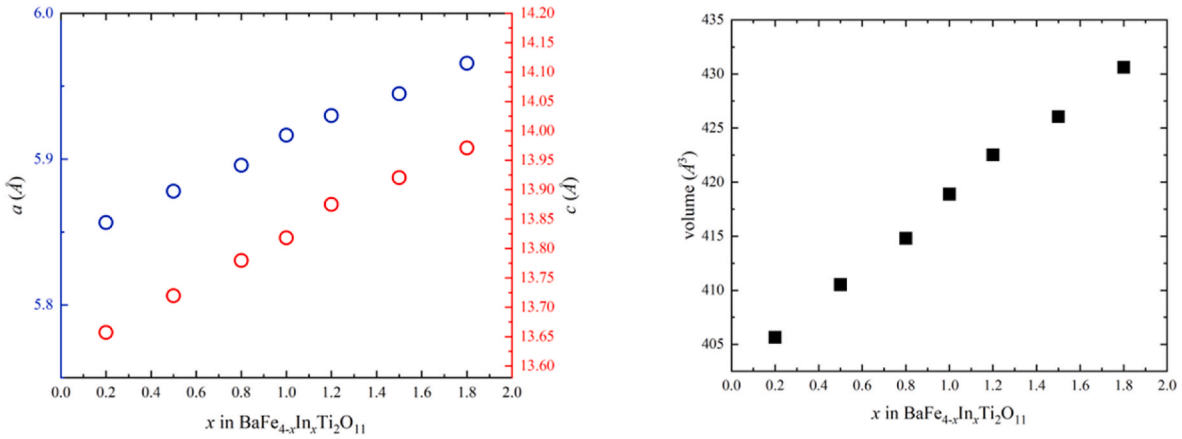

Fig. 3. The variation of lattice parameters and cell volumes with nominal indium content for the new solid solution $BaFe_{4-x}In_xTi_2O_{11}$.

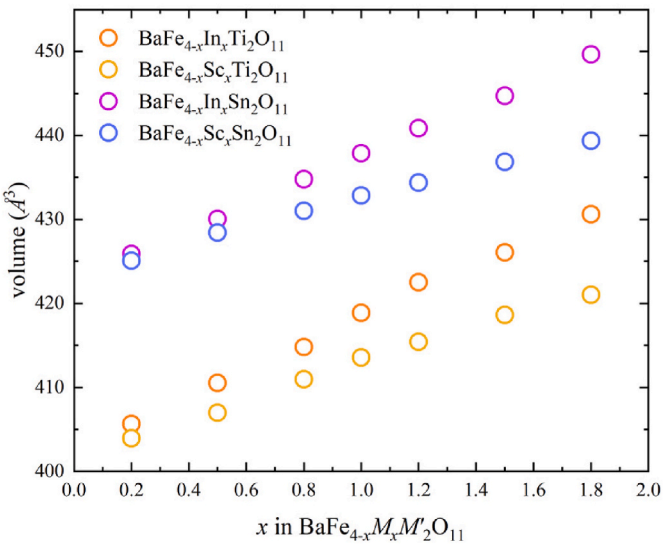

Fig. 4. Comparison of unit cell volumes of $BaFe_{4-x}M_xM'_2O_{11}$ (M = In, Sc; M' = Ti, Sn) solid solutions.

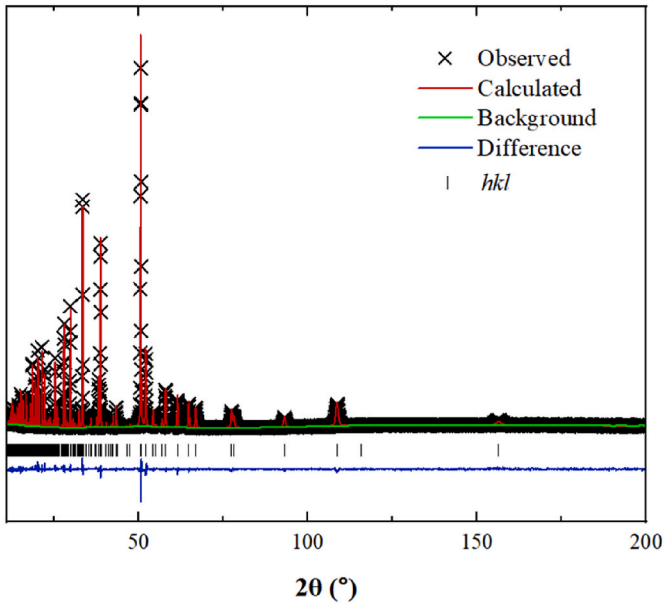

Fig. 5. The Rietveld fitting of the neutron data for $BaFe_{4-x}In_xTi_2O_{11}$ (x = 1.0). The black vertical tick lines indicate the positions of peaks as determined from the hexagonal space-group $P6_3/mmc$.

were collected up to a wavelength of 2500 nm and then converted from diffuse reflectance to absorbance using the Kubelka-Munk equation [19]. The L*a*b* color space data were obtained by Konica Minolta CM-700d spectrophotometer with the standard illuminant D65.

3. Results and discussion

3.1. Structural analysis

Single-phase $BaFe_{4-x}M_xM'_2O_{11}$ (M = In, Sc; M' = Ti, Sn; $0 \le x \le 1.8$) samples were successfully prepared at 1100 °C in the air. The solubility limit of the solid solution is roughly $x = 1.5$. For Fe content below 2.5, a barium indium oxide phase appeared as an impurity. The powder X-ray diffraction patterns are shown in Fig. 2. The lattice parameters and unit cell volumes shown in Figs. 3 and 4 were calculated using LeBail fitting [17]. There are five-fold TBP sites and two distinct six-fold octahedral sites in the crystal structure. Based on Shannon's ionic radii: Fe^{3+}: r (VI) = 0.645 Å; In^{3+}: r (VI) = 0.80 Å; Sc^{3+}: r (VI) = 0.745 Å, the cations of indium and scandium are larger than those of iron, and the lattice parameters and unit cell volumes increase linearly with decreasing iron content as expected (Figs. 3 and 4) [20].

Crystal structures of the new solid solutions $BaFe_{4-x}M_xM'_2O_{11}$ (M = In, Sc; M' = Ti, Sn; $0 \le x \le 1.8$) were refined using neutron diffraction data of selected compositions to study the cation distribution within the system (Fig. 5). Refined crystallographic parameters of $BaFe_3InTi_2O_{11}$ and $BaFe_3InSn_2O_{11}$ are summarized in Table 1. Additional refinement results are included in Tables S1 and S2 in the supporting information. There are three distinct M sites in the R-type hexaferrite structure (S.G.: $P6_3/mmc$), which are M1: face-shared octahedra (*4e*), M2: edge-shared octahedra (*6g*), and M3: TBP (*4f*), as shown in Fig. 6. To improve the Rietveld fit, cations in the TBP sites are shifted from the special position *2d* (1/3, 2/3, 3/4) to *4f* (1/3, 2/3, z), which is slightly above or below the basal plane. The results agree well with the structure data reported in the literature [7]. In the previous study, the cation distribution of $BaFe_4Ti_2O_{11}$ was refined as M1(*4e*): $Fe_{0.55(1)}$, $Ti_{0.45(1)}$; M2(*6g*): $Fe_{0.63(1)}$, $Ti_{0.37(1)}$; M3(*4f*): $Fe_{0.5}$ assuming that the TBP sites are only occupied by Fe [7]. In our neutron refinements, Fe cations in $BaFe_3InTi_2O_{11}$ and $BaFe_3InSn_2O_{11}$ samples remain disordered in both face-shared and edge-shared octahedral sites, while TBP(*4f*) sites are predominantly occupied by Fe. In the case of indium-containing samples, we observe that a small amount of both Ti and Sn are distributed in the TBP(*4f*) sites. The results are shown in Table 1. Our refinements also indicate that both face-shared octahedral and edge-shared octahedral sites are distorted in

Table 1
Crystallographic data refined from powder neutron diffraction [a,b,c].

	$BaFe_3InTi_2O_{11}$	$BaFe_3InSn_2O_{11}$
a (Å)	5.9320(1)	6.0519(1)
c (Å)	13.864(1)	13.880(1)
V (Å^3)	422.49(1)	440.26(1)
wRp (%)	4.67	5.67
$Fe^{3+}/In^{3+}/Ti^{4+}$(*4e*) *z*	0.1434(2)	0.1420(1)
$Fe^{3+}/In^{3+}/Ti^{4+}$(*4f*) *z*	0.7252(1)	0.7297(1)
O (*12k*) *x*	0.1760(1)	0.1762(1)
O (*12k*) *y*	0.3520(2)	0.3525(2)
O (*12k*) *z*	0.0778(1)	0.0795(1)
O' (*6h*) *x*	0.8455(1)	0.8495(1)
O' (*6h*) *y*	0.6910(3)	0.6989(3)
O'' (*4f*) *z*	0.5785(1)	0.5805(1)
Fe^{3+} (*4e*) occup.	0.485(7)	0.116(4)
Fe^{3+} (*6g*) occup.	0.373(5)	0.711(1)
Fe^{3+} (*4f*) occup.	0.435(1)	0.298(3)
In^{3+} (*4e*) occup.	0.146(4)	0.350(4)
In^{3+} (*6g*) occup.	0.249(5)	0.067(1)
In^{3+} (*4f*) occup.	0.000(4)	0.060(3)
Ti^{4+}/Sn^{4+} (*4e*) occup.	0.369(2)	0.531(3)
Ti^{4+}/Sn^{4+} (*6g*) occup.	0.378(1)	0.222(1)
Ti^{4+}/Sn^{4+} (*4f*) occup.	0.064(4)	0.144(3)
BVS of Fe	2.849	2.864

[a] Both crystal structures of samples with the nominal compositions $BaFe_3InTi_2O_{11}$ and $BaFe_3InSn_2O_{11}$ are refined in space group $P6_3/mmc$, where $Fe^{3+}/In^{3+}/Ti^{4+}/Sn^{4+}$ are distributed in the *4e* (0, 0, *z*), *6g* (1/2, 0, 0), and *4f* (1/3, 2/3, *z*), Ba^{2+} is in the *2c* (1/3, 2/3, 1/4), O is in the *12k* (*x*, *y*, *z*) sites, O′ is in the *6h* (*x*, *y*, 1/4), and O″ is in the *4f* (1/3, 2/3, *z*) positions..
[b] The refined formulas for those compositions are $BaFe_{2.96}In_{1.04}Ti_2O_{11}$ and $BaFe_{2.97}In_{1.02}Sn_{2.01}O_{11}$.
[c] Bond valence sum (BVS) of Fe was estimated using VESTA [21].

both compounds (Fig. 6), and the refined formulas are $BaFe_{2.96}In_{1.04}Ti_2O_{11}$ (nominal composition: $BaFe_3InTi_2O_{11}$) and $BaFe_{2.97}In_{1.02}Sn_{2.01}O_{11}$ (nominal composition: $BaFe_3InSn_2O_{11}$). The estimated bond valence sum for the iron cations suggests that the oxidation state of iron in the refined structures is very close to 3.

3.2. Magnetic properties

Iron is the only magnetic species in the $BaFe_{4-x}M_xM'_2O_{11}$ (M = In, Sc; M' = Ti, Sn) system and the magnetization data of the solid solutions are shown in Fig. 7. Here, one sees the end member exhibiting a broad peak at about 90 K, consistent with previous studies that interpreted the increase in susceptibility on cooling as evidence for small-cluster ferrimagnetism [9]. We can see that this broad feature evolves into a sharp peak with temperature-hysteresis at 40 K when the Fe content is reduced by about 20 % in $BaFe_{3.2}Sc_{0.8}Ti_2O_{11}$. Even for 95 % Fe concentration in $BaFe_{3.8}In_{0.2}Ti_2O_{11}$, we find that its broad peak shows hysteresis between zero-field cooled (zfc) and field-cooled (fc) data that is characteristic of spin glass freezing. For 70 % Fe content in $BaFe_{2.8}In_{1.2}Ti_2O_{11}$, the glass transition is at T_g = 25 K, but as with the 20 % compound, we see that temperature hysteresis actually begins above the glass transition, which is an indication that the site mixing between Fe^{3+} and Ti^{4+} is not random, and also consistent with clustering among Fe^{3+} ions. It is interesting to note in this regard that the pseudo brookite phase Fe_2TiO_5 also displays nearly complete site mixing between Fe^{3+} and Ti^{4+} ions but doesn't show hysteresis above T_g [22]. The results are consistent with the behavior in iron hibonite, which also exhibits spin glass freezing [23]. One can also notice that the magnetization above 150 K is very large as if the materials are already in a state of weak ferromagnetism. To assess this state, we show the magnetization vs. field at two different temperatures in Fig. 8. These data confirm the existence of weak ferromagnetism but with low field hysteresis, consistent with the lack of anisotropy in Fe^{3+}, as expected for this spin-only ion.

3.3. Optical properties

The color of the solid solutions $BaFe_{4-x}M_xM'_2O_{11}$ (M = In, Sc; M' = Ti, Sn; $0 \le x \le 1.8$) (Fig. 9) varies from brown to red to yellow hues. The UV–vis diffuse reflectance data of four solid solutions were collected, and reflectance data was converted to absorbance spectra based on Kubelka-Munk (K-M) function, $\boldsymbol{F(R) = (1\text{-}R)^2/2R}$ [19]. In this new *R*-type hexaferrite system, the color of the samples originates from a combination of ligand-to-metal charge transfer (LMCT) and electron pair transitions. The cause of the reddish color in Fe_2O_3 (hematite) has been explained by the charge transfer between the O 2*p* and Fe 3*d* orbitals. The corresponding absorption peak observed around 250 nm extends into the blue region. Electronic transitions in compounds with Fe^{3+} occupying octahedral sites (d^5 electronic configuration) are forbidden due to the spin selection rule. However, the face-sharing of octahedral sites shortens the distance between adjacent Fe cations, enhancing the magnetic interactions and increasing crystal-field intensities. In a magnetically coupled system, the electrons in the adjacent Fe^{3+} cations interact in such a way that magnetic and electronic interactions are coupled. In this case, the spin selection rule can be relaxed via electron pair excitations, as seen in Fe_2O_3 [24,25]. The corresponding absorbance peak can be observed around ~500 nm. In our solid solution samples, this peak intensity decreases as the iron content decreases, which is consistent with our explanation. Consequently, the face-shared octahedral coordination (*4e*) plays a more important role in the observed color than the TBP (*4f*) in our *R*-type solid solutions. However, the structural analyses show that iron chromophores also tend to occupy the TBP sites. The substituents, such as indium and scandium, decrease the concentration of chromophore iron in the face-shared octahedral sites. Consequently, the absorption of the samples shifts toward the blue region with the decreasing iron (Fig. 10). According to the

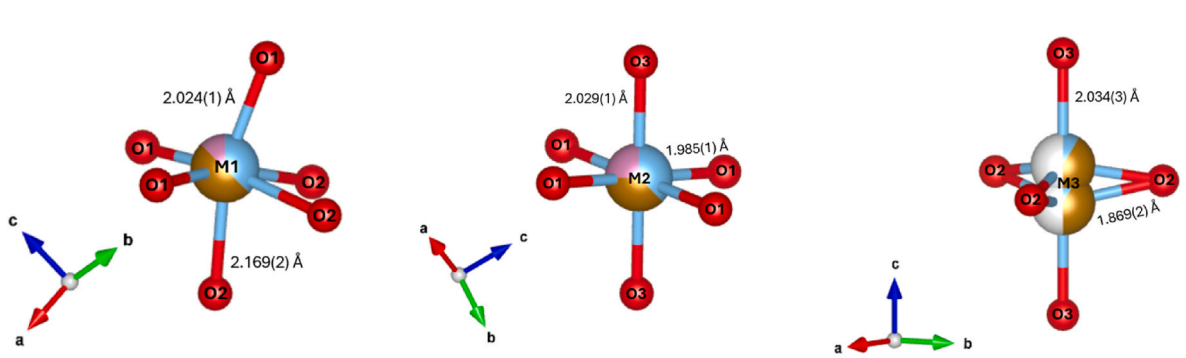

M1: face-shared octahedral (*4e*) M2: edge-shared octahedral (*6g*) M3: TBP (*4f*)

Fig. 6. Three distinct *M* sites in the *R*-type hexaferrite structure and M−O bond lengths refined from neutron diffraction data of $BaFe_3InTi_2O_{11}$. The cation distribution of these *M* sites was refined as M1(*4e*): $Fe_{0.485(7)}$, $In_{0.146(4)}$, $Ti_{0.369(2)}$; M2(*6g*): $Fe_{0.373(5)}$, $In_{0.249(5)}$, $Ti_{0.378(1)}$; M3(*4f*): $Fe_{0.435(1)}$, $In_{0.000(4)}$, $Ti_{0.064(4)}$.

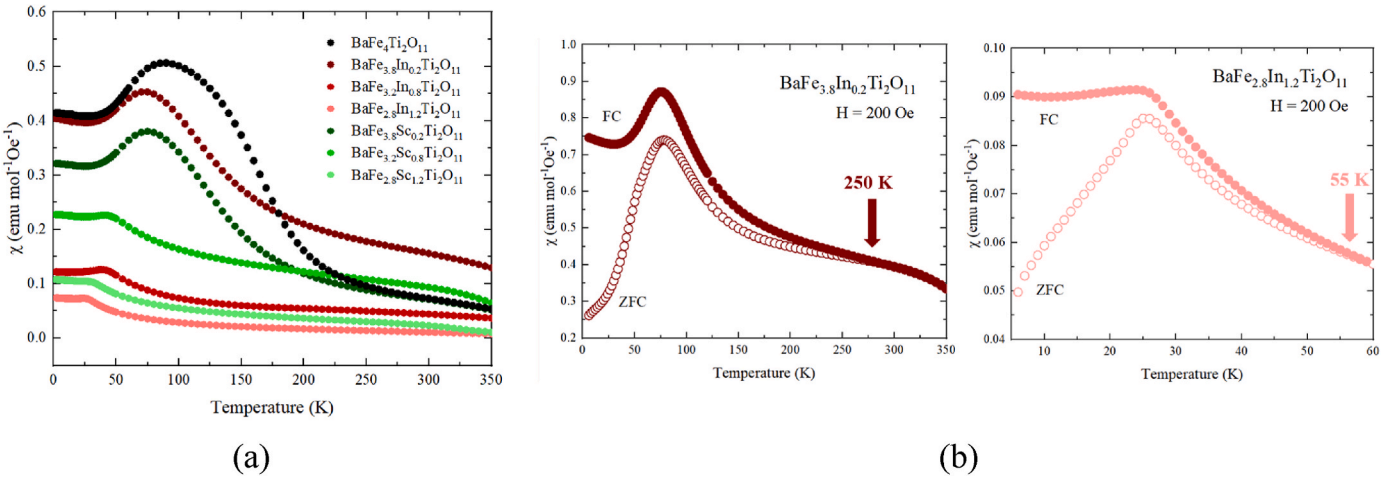

Fig. 7. Magnetization data were obtained from 5 to 300 K (a) Temperature dependence of magnetic susceptibility for $BaFe_{4-x}M_xTi_2O_{11}$ where M = In and Sc. (b) ZFC and FC magnetization curve measurement at 200 Oe DC magnetic field for iron-rich ($BaFe_{3.8}In_{0.2}Ti_2O_{11}$) and iron-less ($BaFe_{2.8}In_{1.2}Ti_2O_{11}$) members.

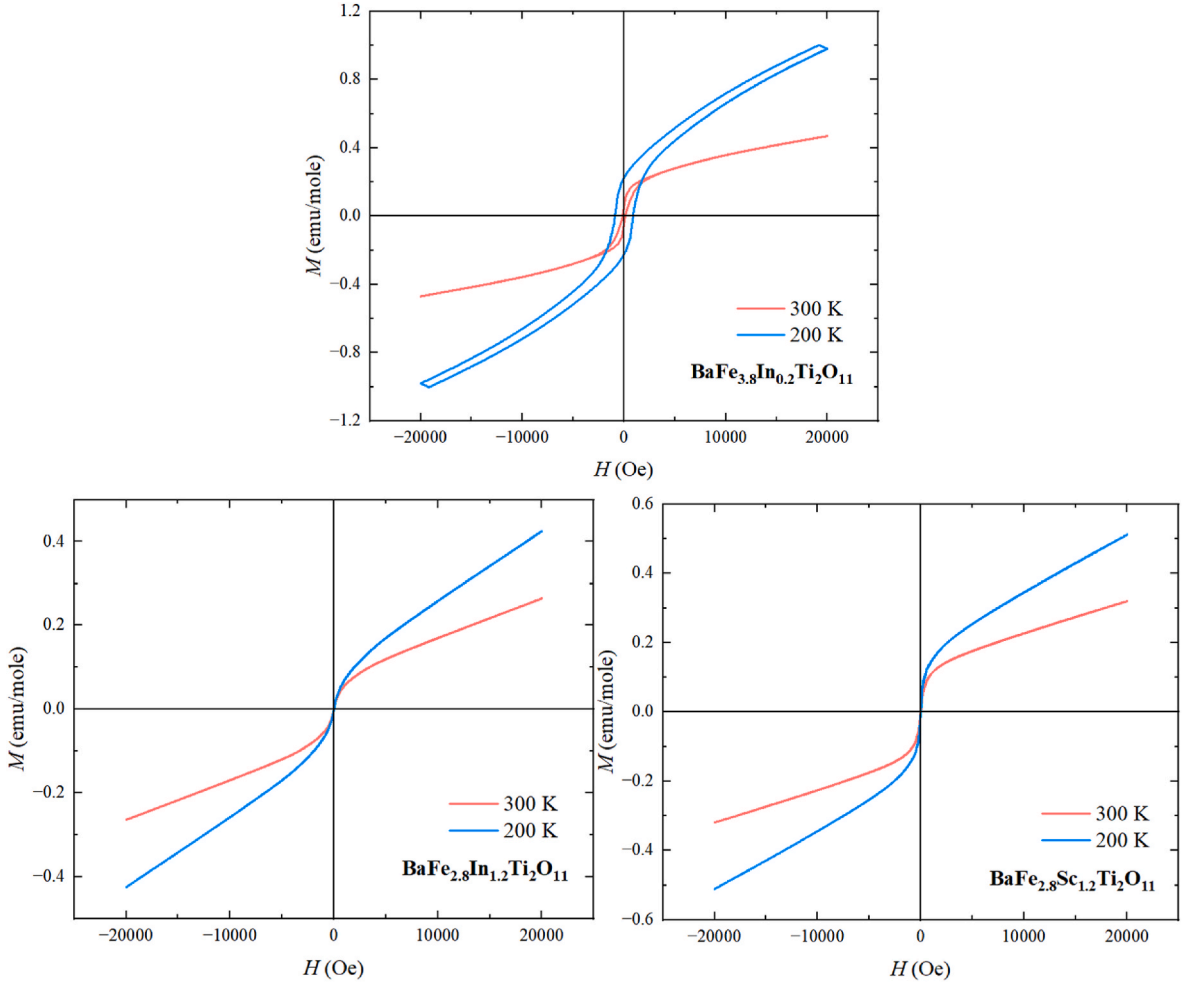

Fig. 8. Magnetic hysteresis loop under 200 °C and 300 °C for $BaFe_{3.8}In_{0.2}Ti_2O_{11}$, $BaFe_{2.8}In_{1.2}Ti_2O_{11}$, and $BaFe_{2.8}Sc_{1.2}Ti_2O_{11}$ between −2 T and 2 T Oe magnetic field. The narrow hysteresis loop refers to the small energy dissipation of the sample.

neutron refinements, iron cations are distributed more in face-shared octahedra (*4e*) in $BaFe_3InTi_2O_{11}$ structure than in $BaFe_3InSn_2O_{11}$. This cation distribution may explain why $BaFe_{4-x}In_xTi_2O_{11}$ samples show more intense colors than those of $BaFe_{4-x}In_xSn_2O_{11}$. Compared to the $CaAl_{9.5}Fe_{2.5}O_{19}$ hibonite sample, which has the reddest hue in the $CaAl_{12-x}M_xO_{19}$ solid solution, the absorption peaks around 500 nm also start showing up after Fe ion becomes concentrated [12]. Both In and Sc exhibited similar behavior in both $BaFe_{4-x}M_xTi_2O_{11}$ and $BaFe_{4-x}M_xSn_2O_{11}$ systems. Their effects on the color changes were not significantly different between In or Sc-containing samples. Both

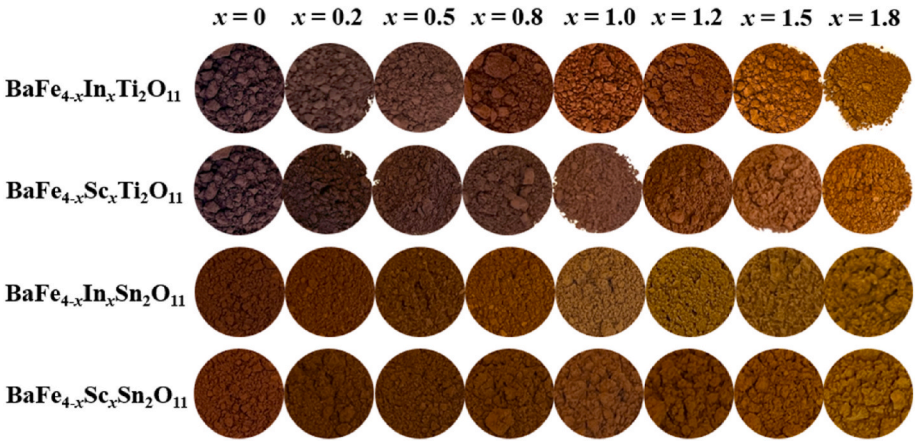

Fig. 9. The corresponding sample colors of the new solid solutions with *R*-type hexaferrite structure, with the nominal composition $BaFe_{4-x}M_xM'_2O_{11}$.

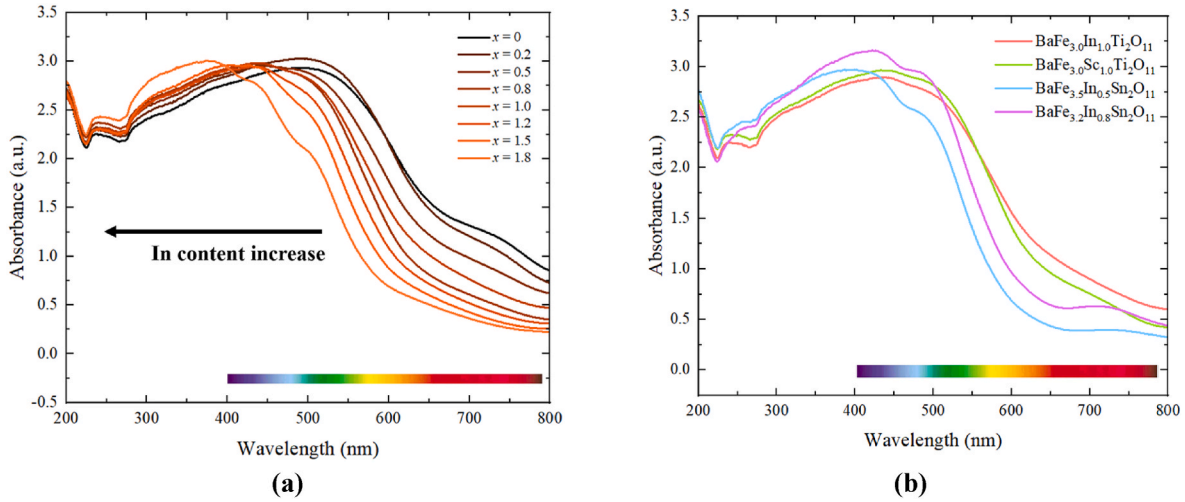

Fig. 10. Absorbance spectra of (a) $BaFe_{4-x}In_xTi_2O_{11}$ solid solutions and (b) reddish compounds from selected new *R*-type hexaferrite compositions $BaFe_{4-x}M_xM'_2O_{11}$ (M = In, Sc; M' = Ti, Sn).

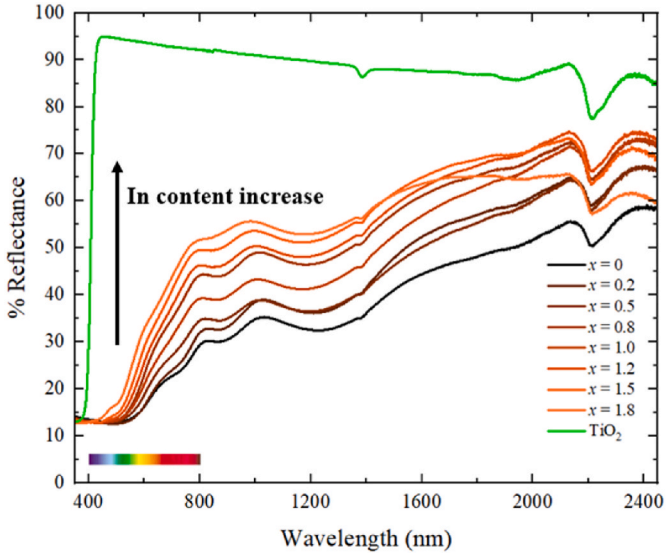

Fig. 11. Near-infrared spectra of $BaFe_{4-x}In_xTi_2O_{11}$ solid solutions.

elements appear to act primarily as diluents for iron content.

High reflectivity in the near-infrared (NIR) region is essential for any pigment to be useful as energy-saving "cool pigments." [26] Fig. 11 shows the diffuse reflectance data of $BaFe_{4-x}In_xTi_2O_{11}$ solid solutions in the range of 700–2500 nm. As you can see, the indium substitution significantly improves the reflectivity of the samples (up to ~70 %) in the NIR region. In fact, all four solid solutions $BaFe_{4-x}M_xM'_2O_{11}$ (M = In, Sc; M' = Ti, Sn) show an increase in the NIR reflectivity when the iron content is decreased by substituting it with indium or scandium. Hence, these new solid solutions with the *R*-type hexaferrite structure can be

Table 2
CIE $L^*a^*b^*$ color coordinates for new *R*-type hexaferrite compositions.

Composition	L^*	a^*	b^*
$BaFe_4Ti_2O_{11}$	27.78	8.27	5.19
$BaFe_{3.8}In_{0.2}Ti_2O_{11}$	28.69	10.50	6.97
$BaFe_{3.5}In_{0.5}Ti_2O_{11}$	29.90	11.81	10.49
$BaFe_{3.2}In_{0.8}Ti_2O_{11}$	33.95	16.00	16.64
$BaFe_{3.0}In_{1.0}Ti_2O_{11}$	31.42	13.85	14.80
$BaFe_{2.8}In_{1.2}Ti_2O_{11}$	36.03	16.09	19.81
$BaFe_{2.5}In_{1.5}Ti_2O_{11}$	37.82	15.99	24.41
$BaFe_{2.2}In_{1.8}Ti_2O_{11}$	42.73	14.21	28.02
$BaFe_{3.0}Sc_{1.0}Ti_2O_{11}$	32.91	15.31	16.52
$BaFe_{3.5}In_{0.5}Sn_2O_{11}$	44.08	19.26	20.97
$BaFe_{3.2}Sc_{0.8}Sn_2O_{11}$	38.67	18.91	26.30

potential candidates as cool pigments [27].

Color can be described and quantified using the CIE $L^*a^*b^*$ color space, defined by the International Commission on Illumination in 1976. The L value refers to black ($L^* = 0$) and white ($L^* = 100$), a^* represented for red ($a^* > 0$)/green ($a^* < 0$) component, and b^* represented for yellow ($b^* > 0$)/blue ($b^* < 0$) component. The color space measurements have been done to evaluate the color of new solid solutions. A Konica Minolta CM-700d color meter was used to measure all the samples. The $L^*a^*b^*$ color coordinating values for $BaFe_{4-x}M_xM'_2O_{11}$ are listed in Table 2. L^*, a^*, and b^* values all increase by diluting the iron content. However, the b^* value increases rapidly when the iron contents are lower than 3.0 and 2.5 in $BaFe_{4-x}In_xTi_2O_{11}$ and $BaFe_{4-x}In_xSn_2O_{11}$ samples, respectively. Thus, the samples become more yellowish instead of turning to more intense red colors. The most reddish samples in the $BaFe_{4-x}M_xM'_2O_{11}$ (M = In, Sc; M' = Ti, Sn) systems are $BaFe_{3.0}In_{1.0}Ti_2O_{11}$, $BaFe_{3.0}Sc_{1.0}Ti_2O_{11}$, $BaFe_{3.5}In_{0.5}Sn_2O_{11}$, $BaFe_{3.2}Sc_{0.8}Sn_2O_{11}$.

4. Conclusion

We have successfully synthesized a series of new solid solutions with a general formula, $BaFe_{4-x}M_xM'_2O_{11}$ (M = In, Sc; M' = Ti, Sn, $0 \leq x \leq 1.8$), and studied their structural, magnetic, and optical properties. Through neutron diffraction refinements, we confirmed that iron is distributed in both octahedral and TBP sites in the hexagonal ferrite structure. The bond valence sum (BVS) calculations for the iron suggest that the oxidation states of iron chromophores are very close to 3. The new compositions show ferrimagnetic behavior and the formation of spin clusters due to the inhomogeneous distribution of iron in various crystallographic sites. A combination of LMCT and electron pair transitions is the reason behind the color of these *R*-type hexaferrite solid solutions. The color of the $BaFe_{4-x}M_xM'_2O_{11}$ samples varies systematically from brown to red to orange/yellow as the x is varied. The new reddish pigments based on the *R*-type ferrite structure show high reflective properties in the near IR region, with a value of around 70 %, indicating potential usefulness in heat-reflecting climate change mitigating coating applications.

CRediT authorship contribution statement

Yu-An Huang: Writing – review & editing, Writing – original draft, Validation, Methodology, Investigation, Data curation, Conceptualization. **Jun Li:** Writing – review & editing, Writing – original draft, Methodology, Investigation, Formal analysis, Data curation, Conceptualization. **Arthur P. Ramirez:** Writing – review & editing, Writing – original draft, Validation, Resources, Methodology, Investigation, Funding acquisition, Formal analysis, Data curation. **M.A. Subramanian:** Writing – review & editing, Writing – original draft, Visualization, Validation, Supervision, Resources, Project administration, Investigation, Funding acquisition, Formal analysis, Conceptualization.

Declaration of competing interest

The authors declare that they have no known competing financial interests or personal relationships that could have appeared to influence the work reported in this paper.

Acknowledgment

The work done at Oregon State University was supported by NSF Grant No. DMR-2025615 (M.A.S.). The work done at UC Santa Cruz (A. P.R.) was supported by NSF Grant No. DMR-2218130. The research used resources at the Spallation Neutron Source (SNS), a DOE Office of Science User Facility operated by the Oak Ridge National Laboratory (ORNL). We thank Dr. Alicia Manjon Sanz for collecting the neutron diffraction data at ORNL.

Appendix A. Supplementary data

Supplementary data to this article can be found online at https://doi.org/10.1016/j.progsolidstchem.2024.100494.

References

[1] Pullar RC. Hexagonal Ferrites: a review of the synthesis, properties and applications of hexaferrite ceramics. Prog Mater Sci 2012;57(7):1191–334. https://doi.org/10.1016/j.pmatsci.2012.04.001.
[2] Singh VP, Jasrotia R, Kumar R, Raizada P, Thakur S, Batoo KM, Singh MA. Current review on the synthesis and magnetic properties of M-type hexaferrites material. World J Condens Matter Phys 2018;8(2):36–61. https://doi.org/10.4236/wjcmp.2018.82004.
[3] Kumar S, Prakash J, Verma A, Jasrotia R. A comprehensive review of synthesis, properties, and applications of $BaFe_{12}O_{19}$ hexaferrites. Mater Today Proc 2023. https://doi.org/10.1016/j.matpr.2023.02.346. S2214785323009100.
[4] Lucena de Medeiros SAS, Menezes de Oliveira AL, Braga GS, Salvador C, Chesman C, da Silva RB, Silva UC, Soledade LEB, dos Santos IMG. M-type hexaferrites $Sr_xBa_{1-x}Fe_{12}O_{19}$ as new magnetic pigments: the role of cationic substitution on the magnetic and colour characteristics. Ceram Int 2022;48(6):8258–67. https://doi.org/10.1016/j.ceramint.2021.12.030.
[5] Huang J, Zhuang H, Li W. Synthesis and characterization of nano crystalline $BaFe_{12}O_{19}$ powders by low temperature combustion. Mater Res Bull 2003;38(1):149–59. https://doi.org/10.1016/S0025-5408(02)00979-0.
[6] Hajjaji W, Pullar RC, Zanelli C, Seabra MP, Dondi M, Labrincha JA. Compositional and chromatic properties of strontium hexaferrite as pigment for ceramic bodies and alternative synthesis from wiredrawing sludge. Dyes Pigments 2013;96(3):659–64. https://doi.org/10.1016/j.dyepig.2012.10.011.
[7] Obradors, X.; Isalgu, A.; Tejada, J.; Joubert, J. C. Crystal structure and cationic distribution of $BaFe_4Ti_2O_{11}$ R-type hexagonal ferrite. vol. 18 (12), 11.
[8] Obradors X, Isalgué A, Collomb A, Pernet M, Tejada J, Joubert JC. Magnetic properties of $BaFe_4Mn_2O_{11}$ R-type hexagonal ferrite. J Phys Colloq 1985;46(C6). https://doi.org/10.1051/jphyscol:1985662. C6-339-C6-343.
[9] Kneller E, Velicescu M, Haberey F. Spin structure and magnetic properties of the R-type hexaferrite $BaFe_4Ti_2O_{11}$. J Magn Magn Mater 1978;7(1–4):49–51. https://doi.org/10.1016/0304-8853(78)90147-6.
[10] Duell BA, Li J, Subramanian MA. Hibonite Blue: a new class of intense inorganic blue colorants. ACS Omega 2019;4(26):22114–8. https://doi.org/10.1021/acsomega.9b03255.
[11] Li J, Medina EA, Stalick JK, Sleight AW, Subramanian MA. Colored oxides with hibonite structure: a potential route to non-cobalt blue pigments. Prog Solid State Chem 2016;44(4):107–22. https://doi.org/10.1016/j.progsolidstchem.2016.11.001.
[12] Medina EA, Li J, Subramanian MA. Colored oxides with hibonite structure II: structural and optical properties of $CaAl_{12}O_{19}$-type pigments with chromophores based on Fe, Mn, Cr and Cu. Prog Solid State Chem 2017;45–46:9–29. https://doi.org/10.1016/j.progsolidstchem.2017.02.002.
[13] Laporte O, Meggers WF. Some rules of spectral structure. J Opt Soc Am 1925;11(5):459. https://doi.org/10.1364/JOSA.11.000459.
[14] Smith AE, Mizoguchi H, Delaney K, Spaldin NA, Sleight AW, Subramanian MA. Mn^{3+} in trigonal bipyramidal coordination: a new blue chromophore. J Am Chem Soc 2009;131(47):17084–6. https://doi.org/10.1021/ja9080666.
[15] Subramanian MA, Li J. YInMn Blue - 200 Years in the making: new intense inorganic pigments based on chromophores in trigonal bipyramidal coordination. Mater Today Adv 2022;16:100323. https://doi.org/10.1016/j.mtadv.2022.100323.
[16] Li J, Subramanian MA. Inorganic pigments with transition metal chromophores at trigonal bipyramidal coordination: $Y(In,Mn)O_3$ blues and beyond. J Solid State Chem 2019;272:9–20. https://doi.org/10.1016/j.jssc.2019.01.019.
[17] Toby BH. EXPGUI , A graphical user interface for *GSAS*. J Appl Crystallogr 2001;34(2):210–3. https://doi.org/10.1107/S0021889801002242.
[18] Larson AC, Von Dreele RB. General structure analysis system (GSAS). Los Alamos, NM: Los Alamos National Laboratory Report LAUR; 2004, 87545.
[19] Kubelka Paul, Munk Franz. An article on optics of paint layers. Z Tech Phys 1931;12(593–601):259–74.
[20] Shannon RD. Revised effective ionic radii and systematic studies of interatomic distances in halides and chalcogenides. Acta Crystallogr Sect A 1976;32(5):751–67. https://doi.org/10.1107/S0567739476001551.
[21] Momma K, Izumi F. *Vesta* : a three-dimensional visualization system for electronic and structural analysis. J Appl Crystallogr 2008;41(3):653–8. https://doi.org/10.1107/S0021889808012016.
[22] LaBarre PG, Phelan D, Xin Y, Ye F, Besara T, Siegrist T, Syzranov SV, Rosenkranz S, Ramirez AP. Fluctuation-induced interactions and the spin-glass transition in Fe_2TiO_5. Phys Rev B 2021;103(22):L220404. https://doi.org/10.1103/PhysRevB.103.L220404.
[23] Duell BA, Li J, LaBarre PG, Zhang JJ, Hermann RP, Ramirez AP, Subramanian MA. Structure and electronic properties of $CaAl_{12-x}Fe_xO_{19}$ hibonites. J Solid State Chem 2020;291:121650. https://doi.org/10.1016/j.jssc.2020.121650.
[24] Tilley RJD. Colour and the optical properties of materials: an exploration of the relationship between light, the optical properties of materials and colour. 1st ed.; Wiley, https://doi.org/10.1002/9780470974773; 2010.

[25] Jiang Z, Liu Q, Roberts AP, Dekkers MJ, Barrón V, Torrent J, Li S. The magnetic and color reflectance properties of hematite: from earth to mars. Rev Geophys 2022;60(1):e2020RG000698. https://doi.org/10.1029/2020RG000698.
[26] Jose S, Joshy D, Narendranath SB, Periyat P. Recent advances in infrared reflective inorganic pigments. Sol Energy Mater Sol Cells 2019;194:7–27. https://doi.org/10.1016/j.solmat.2019.01.037.
[27] Jeevanandam P, Mulukutla RS, Phillips M, Chaudhuri S, Erickson LE, Klabunde KJ. Near infrared reflectance properties of metal oxide nanoparticles. J Phys Chem C 2007;111(5):1912–8. https://doi.org/10.1021/jp066363o.